The role of compressive stresses in jointing on Vancouver Island, British Columbia

Brad Bessinger[a,*], Neville G.W. Cook[b], Larry Myer[c], Seiji Nakagawa[c], Kurt Nihei[c], Pascual Benito[b], Roberto Suarez-Rivera[c]

[a]*Department of Water Resources, URS Corporation, 500 12th Street, Suite 200, Oakland, CA 94710, USA*
[b]*Department of Materials Science and Mineral Engineering, University of California at Berkeley, Berkeley, CA 94720, USA*
[c]*Earth Sciences Division, Lawrence Berkeley National Laboratory, 1 Cyclotron Road, Berkeley, CA 94720, USA*

Abstract

This study demonstrates that joint-parallel compressive stresses were integral to the development of joint sets on Vancouver Island, British Columbia. The mapped study area contains paleostress indicators in the form of calcareous concretions, which have multiple, internal fractures in precisely the same orientation as one of the surrounding joint sets in the sandstone matrix. Field and laboratory tests indicate that the stiffest concretions are the most likely to be fractured; however, results from numerical simulations using measured rock properties preclude an origin for the concretion fractures from either a far-field uniaxial tensile or compressive stress. Fracturing is only found to be possible if the concretions possessed a lower Poisson's ratio than the sandstone at the time of fracturing. In the latter case, a far-field uniaxial compressive stress may have generated tensile effective stresses in the vicinity of high modulus concretions, seeding the field site with an initial population of concretion fractures and joints. Given the close spacing of some joints, their extension cannot be satisfactorily explained without invoking grain-scale compression-driven tensile fracturing mechanisms.
© 2002 Elsevier Science Ltd. All rights reserved.

Keywords: Compressive stresses; Jointing; Paleostress indicators

1. Introduction

Joints are a distinct *mode* of geologic fracture, distinguished from faults in that the displacement that occurs across the fracture interface is a dilation. Because joints often occur in parallel trending sets of closely-spaced fractures, they can control the mechanical and hydraulic properties of the enclosing rock mass. Consequently, joints affect erosion and structural lineaments in continents (Nur, 1982), the productivity of oil and natural gas reservoirs (Huang and Angelier, 1989), and the stability of underground excavations (Goodman, 1993).

Despite the fact that stresses in the Earth are predominantly compressive, several scenarios have been devised to account for the occurrence of tensile effective stresses required for jointing (Pollard and Aydin, 1988). For example, tension can develop in a sedimentary basin during burial below the chord of the earth, or renewed uplift, where

plate flexure occurs (Price and Cosgrove, 1990). Tensile stresses may also develop along the crest of folds (Nur, 1982; Kemeny and Cook, 1985), or where thermal or mechanical strains are applied to a layered sequence of differing elastic properties (Suppe, 1985; Wu and Pollard, 1995). Finally, tensile effective stresses are possible in a buried rock mass due to porewater pressure (Secor, 1965).

Although mechanisms that rely on far-field tensile stresses or pore water pressures have been successfully employed to explain many small-scale features of joints (e.g. Cruikshank et al., 1991), there are two fundamental limitations restricting their geologic importance. The first is that they do not adequately characterize one of the most important properties from a geological and engineering perspective—the clustering of joints into zones of closely-spaced fractures (Huang and Angelier, 1989; Olson, 1993). Pollard and Segall (1987) demonstrated that the dilation of an opening mode crack disrupts the surrounding stress field so that the tensile crack driving stress is only 72% of its remote value at one crack length away. This stress shadow not only makes it improbable for incipient joints to form

* Corresponding author.
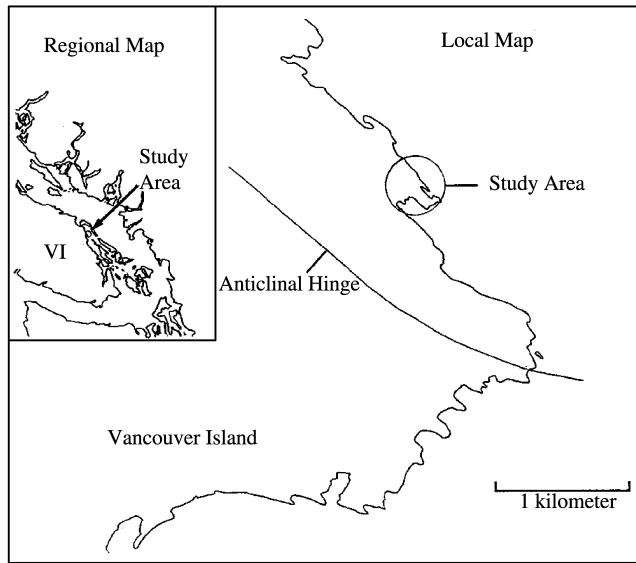*E-mail address:* brad_bessinger@urscorp.com (B. Bessinger).

Fig. 1. Location of field site on southern Vancouver Island, British Columbia. The study area is located within the circled region of the figure on a 400 m stretch of coastline.

closer than the length of a pre-existing discontinuity in bedded rock in which joints are confined to a single layer (Bai and Pollard, 2000), but also makes joint zones even more unlikely if either bedding planes are not completely welded or joints in adjoining layers contribute to it.

The second fundamental problem is that hydraulic fracturing, which is used to explain the observations of joint sets in the absence of obvious deformation, may be less important than previously recognized because the last term in Eq. (1) is often wrongly neglected (Engelder and Lacazette, 1990). Assuming uniaxial strain boundary conditions during burial of a sedimentary basin, the confining stress (σ_3) is given by:

$$\sigma_3 = \left(\frac{\nu}{1-\nu}\right)(\sigma_1 - \alpha p) + \alpha p \qquad (1)$$

where (σ_1) is the gravitational loading stress, (ν) is the Poisson's value, (α) is a constant relating the loading stress to hydrostatic stress, and the compressive stress and fluid pressure (p) are positive. Although an increase in (αp) reduces the effective stress, it also contributes to the confining stress (σ_3), such that the effective confining stress (σ_3') is given by:

$$\sigma_3' = \sigma_3 - \alpha p \qquad (2)$$

and

$$\sigma_3' = \left(\frac{\nu}{1-\nu}\right)(\sigma_1 - \alpha p). \qquad (3)$$

Assuming that (α) is equal to one, for the effective confining stress to become tensile (i.e. negative) to propagate a joint, the fluid pressure must exceed the overburden stress. This is inconsistent with observations in deep basins (Lorenz et al., 1991).

Considering the limitations of current theories, an alternative jointing mechanism is that joint parallel compressive stresses generate joint perpendicular tensile stresses in the vicinity of field or grain-scale inhomogeneities in rock. Eidelman and Reches (1992) previously hypothesized such a mechanism for fractured pebbles observed in the field. Also, Jaeger and Cook (1963) showed that biaxial compressive stresses can cause subparallel tensile fracturing in cylindrical rock cores. Finally, Kemeny and Cook (1987) formulated mathematical models describing the interaction and coalescence of microcracks into macroscopic opening-mode fractures under uniaxial compressive stresses.

The objective of this study is to resolve the relative importance of compression-driven tensile fracturing mechanisms during jointing at a field site on Vancouver Island, British Columbia. Field observations and measurements of the jointed site are compared with model predictions for the failure of rock under both tensile and compressive uniaxial stresses to determine which mechanism is most compatible with the data.

2. Geologic background

2.1. Geologic setting

The field site selected for this study is located along a beach on southeastern Vancouver Island, British Columbia, within the circled region in Fig. 1. The dominant structural feature of the region is the Cowichan Fold and Thrust System (CFTS), which covers an approximate area of 140×60 km, and completely encompasses the field site (England and Calon, 1991). The observations and measurements of this study are from a site located approximately 1 km northeast of an anticlinal hinge. Although no thrust faults are observed in the study area, right lateral strike-slip faults occur within a 10 km radius (England and Calon, 1991). The fact that these faults cut across the CFTS suggests they post-date this deformation.

2.2. Geologic history

The field site is part of a sandstone and conglomerate sedimentary succession known as the DeCourcy Formation, which was originally deposited between 77.5 and 76.5 Ma, in either a forearc (England, 1990) or foreland basin (Mustard, 1994) along the western edge of North America. This basin remained active until 66.5 Ma, resulting in an additional 3 km of sedimentation (Mustard, 1994) and a total tectonic subsidence of 2.7 km. Although little information is available on the fate of the DeCourcy Formation during the Paleocene (65–54 Ma), development of the CFTS occurred at the close of the Eocene (42–38 Ma), subsequently folding and faulting all of the
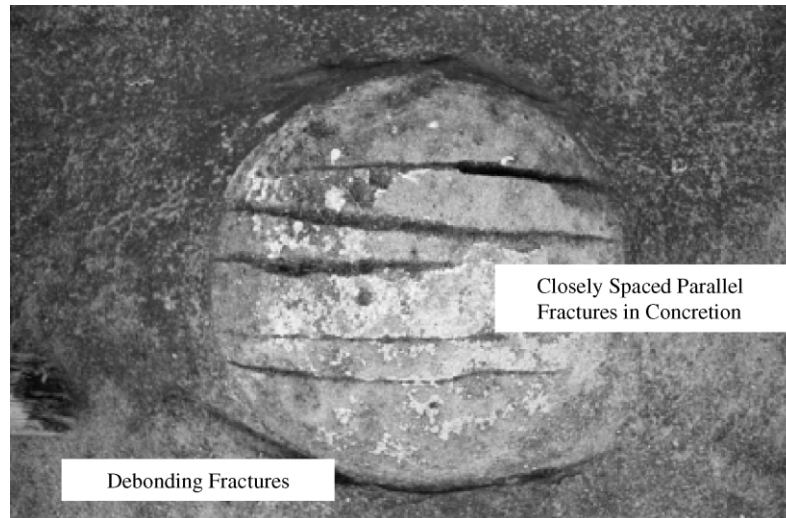
Fig. 2. An example of the morphology of a concretion and its fractures. This photograph represents concretion #9 of Area 9 (see Fig. 14). The concretion is nearly spherical and protrudes from the surrounding sandstone. There are multiple fractures in the concretion, all in the direction of joint set #1. In addition to the internal fractures, the concretion has fractures along its contact with the sandstone (identified as debonding fractures in the figure).

sedimentary units in the Nanaimo Group and initiating the uplift of sedimentary strata which continues today.

3. Field observations

3.1. Sediment description

Field observations are from a 400×10 m coastal outcrop of gently dipping DeCourcy Formation sandstone. The strike of the jointed sandstone unit is between S40°E and S50°E, and is subparallel to the trend of a nearby anticline (Fig. 1). Because bedding does not dip significantly over the interval of the study area, a single bedding plane is exposed over the entire length of the beach. The sandstone unit is characterized by the presence of spherical to ellipsoidal calcareous concretions, which range in size from 0.1 to 3 m and often protrude from the surrounding matrix because they better resist erosion. An example of a fractured concretion is shown in Fig. 2. Although the boundary between many concretions and sandstone is distinct, some exhibit rims of discolored matrix material adjacent to them. Petrographic analyses indicate that these rims have intermediate calcite concentrations (Bessinger, 2000).

3.2. Observations of sandstone fractures

The field site was mapped along a 5–6-m-wide scan line for 260 m of its length (Fig. 3). Because the strike of the beach in which the joints are located varies slightly (from S40°E to S50°E), the strike for any particular 30-m-section is shown at the top of each interval in the figure. The most notable exception to the sectioned mapping is the missing area between 15 and 30 m, an area that is partially infilled by water even during low tide, and that has been previously disturbed by blasting (this precluded testing the rock properties in this area, which was the purpose of the scanline).

Fractures along the scanline and distributed concretions along the beach are shown in Fig. 3 (the latter can be identified by their circular to elliptical shapes). Where either a slight discoloration of the sandstone or an erosional rim was observed surrounding a concretion, a dashed line was drawn. In cases where fractures were obscured, dashed lines were also used to indicate inferred fracture orientations. This is most evident in the fracture zone at 55 m. Although fractures in the sandstone matrix are relatively diffuse, intense fracture zones are present in some locations (especially in Areas 1 and 2). By contrast, concretions are generally more heavily fractured than the sandstone, with fracturing especially pronounced in Area 4.

There are three dominant joint sets in both the concretions and sandstone, identified by taking a random sampling of 120 sandstone and 60 concretion fracture orientations (Fig. 4). The most dominant fracture set roughly parallels the strike of the beach and the anticlinal axis, while the two other fracture sets are more oblique. The most interesting result in the figure is that the fractures in the concretions coincide with one or more fracture sets in the sandstone. This suggests they likely formed in the same stress field.

The sandstone fractures belonging to set #1 are generally linear and parallel. Because no mode II displacement is evident, these fractures are likely *joints*. Additional mapping of joint set #1 was performed in two locations where vertical cross-sections were available. Fig. 5a is a more extensive map of the Area 1 scanline with joint spacing measured along the line A–A'. Joint spacing was also measured in Area 10, slightly offset from the scanline of Fig. 3, across the B–B' scanline of Fig. 5b. Joint spacing
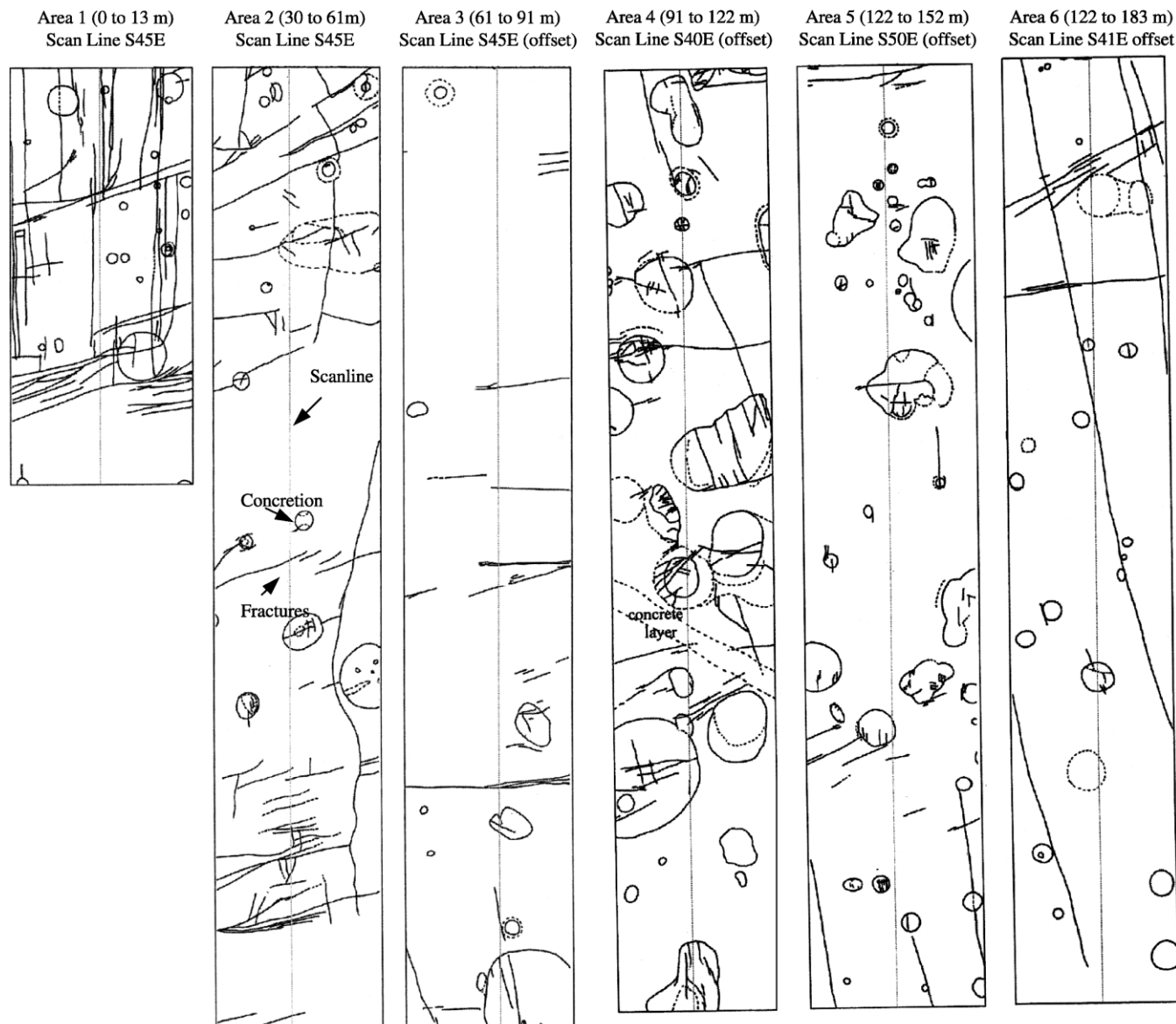
Fig. 3. The mapped section of the field site along the strike of the beach. The strike for any section is given at the top of each plot. The length along the strike is indicated on the right of each figure. (a) Area 1 is densely fractured with two dominant fracture sets. Dense erosion has occurred within the set perpendicular to the strike. Some of these fractures are braided and may represent a shear zone. Multiple concretions can be identified by their circular shapes. (b) The first 9 m of Area 2 is at tide level and is deeply eroded. The fracture that runs from 41 to 56 m is actually a ledge now, but may have initiated at the edge of the large concretion at 49–50 m. Another fracture zone is evident between 53 and 55 m. Not all of the fractures could be identified and have been drawn with dashed lines. (c) Area 3 is not as heavily fractured and also contains fewer concretions. (d) Area 4 contains many, large concretions which are also densely fractured. By contrast, the sandstone is not heavily jointed. Concretion rims are drawn with dashed lines surrounding some concretions. (e) Many of the concretions of Area 5 are not spherical. Fracturing is again concentrated near the concretions. (f) One fracture zone is evident at 154–157 m in Area 6. Several, very long joints of set #1 cut across this area at a regular spacing. The concretions are not heavily fractured. (g) Two fracture sets occur in Area 7. There are few concretions. (h) Fracturing in Area 8 is predominantly constrained to the concretions. Debonding along some concretions has occurred and multiple, internal fractures within the concretions are also present. (i) Area 9 contains the concretion in Fig. 2. Several, long debonding fractures have become joints in the sandstone.

is considerably closer than the height of exposed bed thickness, and exhibits a trend opposite to the distribution predicted using the tensile driving stress equations of Pollard and Segall (1987) (Fig. 6).

Fracture sets #2 and #3 most commonly display the same linearity and lack of discernible dilation as joint set #1;

however, some fractures also have measurable mode II offset. Shear displacement is most noticeable in the region along the scanline between 15 and 30 m where right-lateral horsetail features and left-lateral en échelon jointing is present. It is possible that fracture sets #2 and #3 were originally joints that were later sheared (Segall and Pollard, 1983). The fact that

there are many unsheared fractures belonging to sets #2 and #3, and the morphology of these unsheared fractures is similar to joint set #1, supports this hypothesis.

The relative ages of the *joint* sets were not determined because no systematic cross-cutting relationships were identified. Renshaw and Pollard (1995) showed that for the case where pre-existing joints are closed, younger joints may intersect rather than terminate against older joints.

3.3. Observations of concretion fractures

Fractures in embedded concretions are more complex than those in the sandstone matrix, and are classified in this study as Type 1 or Type 2, depending on the fracture morphology they exhibit. Type 1 concretions are either unfractured or fractured by a sandstone joint, but show no evidence that joint propagation was influenced by the concretion. Type 2 concretions are characterized by fractures either within concretion and/or at their boundary with the sandstone. The latter are identified as 'debonding fractures' in Fig. 2. The amount of dilation of Type 2 concretion fractures is highly variable, ranging from grain-scale to centimeters.

4. Field measurements

4.1. Field methods

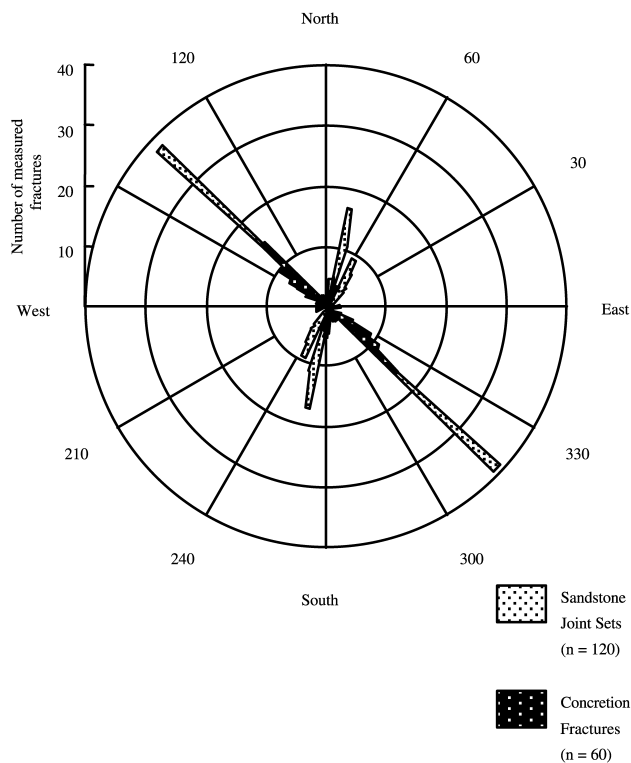A portable nondestructive testing device called a

Fig. 3 (*continued*)

Fig. 4. The orientation of a random sampling of 120 joints and 60 concretion fractures. The joint sets and concretion fractures have precisely the same orientation. Joint set #1 is roughly parallel to the anticlinal hinge of Fig. 1.

Schmidt hammer was used to record the mechanical properties of the sandstone and concretions. The hammer measures the rebound of a plunger mass with the rock, the impact of which can be treated as an inelastic collision described by the laws of conservation of mechanical energy and conservation of linear momentum to be:

$$k = -\frac{v_2}{v_2} = \sqrt{\frac{h_2}{h_1}} \tag{4}$$

where k is the coefficient of restitution, v_1 and h_1 are the impact velocity and height, and v_2 and h_2 are the rebound velocity and height (Hucka, 1965). The coefficient of restitution has also been called the coefficient of dynamic elasticity, and the value for a particular impact is governed mostly by the properties of the softer material. Because v_1 and h_1 are functions of the test hammer, the relative rebound height for the N-type hammer is a measure of the surface hardness of the rock being impacted. The maximum rebound value recorded by the Schmidt hammer ranges from 0 to 100, indicating the percent of the forward distance the mass rebounded.

Many different Schmidt hammer measurement techniques have been conceived (Atkinson, 1978; Poole and Farmer, 1980), but the method selected for this study was to take seven consecutive hits at any one location, discard the first two impacts, and average the three middle values. Although the initial impacts may have caused some compaction, it is
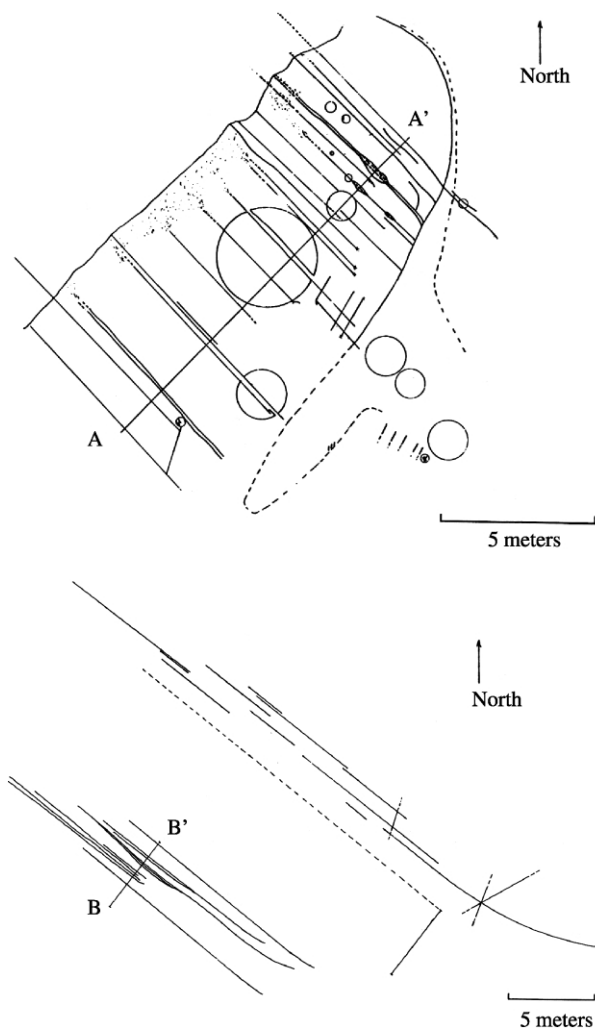

Fig. 5. (a) An extended map of Area 1, with portions not shown in Fig. 3. The scanline A–A′ was used to measure fracture spacing versus the exposed bedding depth of 1.2 m. Because bedding was massive, the depth of this particular bedding may be thicker than can be observed. (b) Map of Area 10 slightly offset from Area 9. The joints in this figure are very closely-spaced and linear for most of their lengths. The joints constrained by line B–B′ actually lie across B–B′ in the joint zone to the right. Fracture spacing measurements were also made along this line. The long dashed line parallel to the joints represents a ledge. The crossed lines at the end of the joint zone on the right represents the other two fracture sets of the region. Southeast of Area 10, along the strike of the beach, the fractures become extremely dense.

justified on the basis that the first two impacts were highly variable and were lower than the remaining five (Fig. 7). Impacts were made every three feet (0.91 m) along the scanline of Fig. 3 to measure the variation in sandstone properties, and within and adjacent to each concretion to measure the contrast in properties between the two lithologic units. To account for the ISRM recommendation that no cracks should be present within 6 cm depth, all impacts that produced a low frequency resonance were considered to have sampled delamination of the sandstone and were removed from further consideration (the bottom curve in Fig. 7a shows the justification for this procedure).
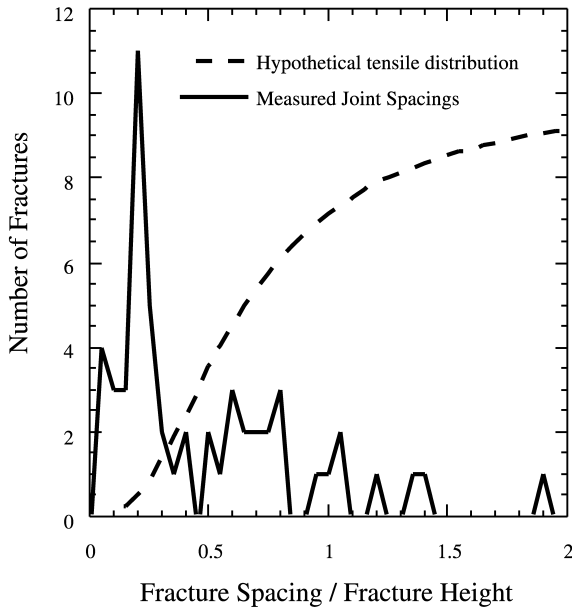
Fig. 6. The results of the joint spacing measurements versus exposed bedding height. Most joints are spaced much closer than the bedding height. A hypothetical joint distribution for joints formed in a uniaxial tensile stress field is represented by the solid line. The shape of the curve is based on the predictions of Pollard and Segall (1987) described in the text.

One possible source of measurement error that had to be accounted for in this study is the potential for Schmidt rebound values to decline with use due to a build-up of metal filings in the hammer (this increases friction and damping) (McCarroll, 1987). Fig. 8 shows the distribution of Schmidt hammer rebound values for the sandstone matrix with time (the gaps are due to concretion impacts). The mean sandstone values actually increase slightly because Areas 1 and 2, which have rebounds lower than the mean, were measured first. Consequently, this source of measurement error is unlikely to be important.

4.2. Measurement of sandstone rebound values

To identify relationships between sandstone Schmidt readings and fractures at the field site, fracture densities were assigned at each Schmidt hammer measurement location along the scanline based on measurements in a 3.3 m^2 area encompassing the point. According to the results of an *F*-statistical test using individual points subdivided by fracture densities greater or less than that 0.23 m/m^2, the means and standard deviations of Schmidt hammer readings between relatively fractured and unfractured sandstone are different. This result is illustrated graphically in Fig. 9, which shows a comparison between average rebound value of fractured areas along the scanline to the average rebound values of relatively unfractured sandstone on either side. Almost all of the unfractured areas have higher Schmidt values than their adjacent fracture
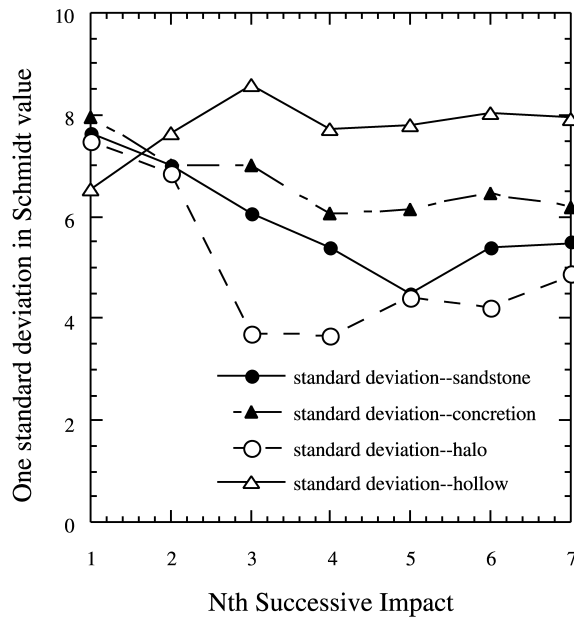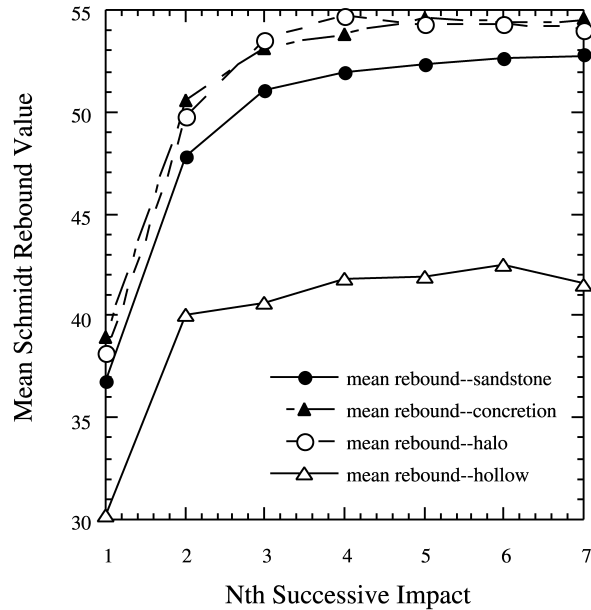

Fig. 7. (a) Distribution of mean Schmidt rebound values as a function of the number of successive impacts at any one point. The first two impacts are lower than the remaining impacts and represent densification and smoothing of the rough sandstone surface. The highest rebound values are for the concretions and surrounding rims. Very low numbers are recorded for delaminated sandstone. (b) The variance in rebound values with successive impact. Standard deviations decrease with each impact except for the case of the delaminated sandstone.

zones. The only exception is the highly fractured Area 1, where the entire area has low Schmidt values.

4.3. Measurement of concretion rebound values

The means and standard deviations of Schmidt values from Type 1 and 2 concretions were similarly found via an *F*-statistical test to represent different subpopulations. This
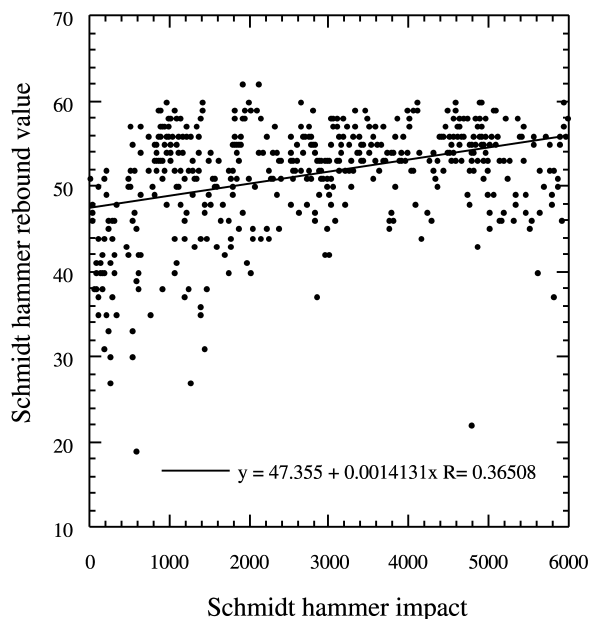
Fig. 8. Distribution of mean Schmidt rebound values within the sandstone as a function of time. The gaps in measurements in the figure represent concretion impacts. The overall trend of Schmidt values increases with time (see text for explanation).

result is illustrated graphically in Fig. 10, which shows the distribution of concretion Schmidt values for each concretion, and the ratio between the concretion and adjacent sandstone. The fractured concretions in the figure generally have higher Schmidt values and higher Schmidt values relative to the surrounding sandstone. Although this positive correlation between concretion hardness and fracture density is *opposite* to the sandstone, and *opposite* to what might be expected if increased weathering in the vicinity of
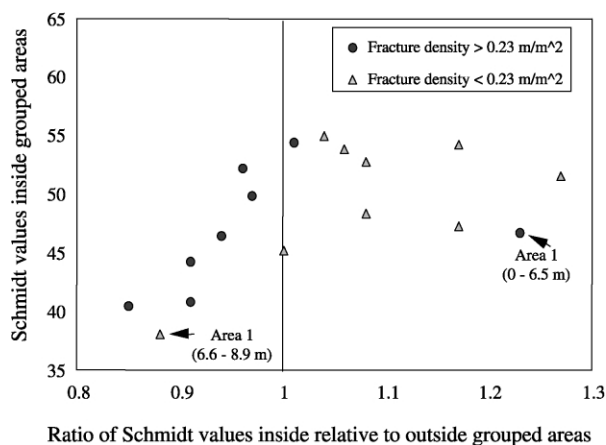

Fig. 9. Comparison of mean Schmidt rebound numbers for different regions of the study area grouped together by their fracture densities. For example, Area 1 (0–5 m) represents a relatively unfractured region (fracture density < 0.23 m/m^2) surrounded by two regions with fracture densities greater than 0.23 m/m^2. The mean Schmidt value for any region is shown along the vertical axis and the ratio of the mean value to the surrounding two regions along the horizontal axis. Except for two regions in Area 1, the largest Schmidt rebound number and ratios occur for the unfractured regions.
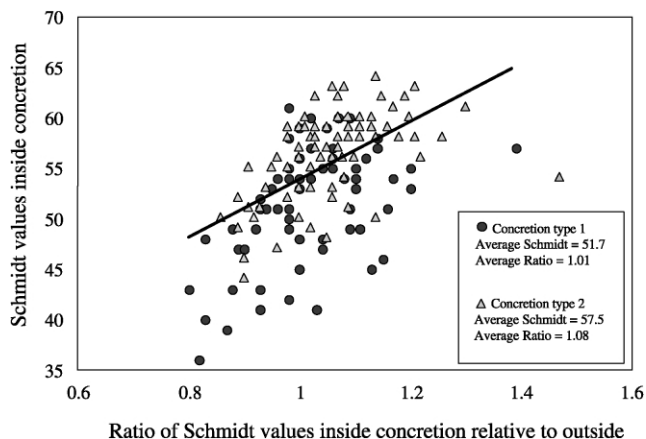

Fig. 10. Comparison of the mean Schmidt rebound values of 'unfractured' (Type 1) and fractured (Type 2) concretions. The vertical axis is the mean value and the horizontal axis the ratio of the mean value measured within and outside of the concretion. The fractured concretions have both the highest Schmidt values and ratios. This result is exactly the *opposite* of the sandstone in Fig. 9.

concretion fractures produce lower Schmidt readings, it is consistent with stiffer concretions concentrating geologic stresses in excess of their strength.

5. Laboratory measurements

5.1. Laboratory methods

Because hardness values cannot be used as input into analytical and numerical models, a series of laboratory experiments were performed using 0.1-m-diameter cores drilled from four concretions and the adjacent sandstone. Elastic moduli and compressive strengths were determined from uniaxial compression tests, and tensile strengths inferred from Brazilian tests (Tables 1 and 2, respectively). Concretion sample C1 is an unfractured Type 1 concretion, and samples C2–C4 are fractured Type 2 concretions. Sandstone sample S3 is from a rim of partially calcite-cemented sandstone surrounding a concretion.

5.2. Uniaxial compression tests

The third column of Table 1 shows the height to diameter ratios of the cores used in the uniaxial tests. These ratios are smaller than the 2.5–3.0 recommended by the ISRM (Bieniawski, 1979). Consequently, it is likely that the steel end platens interacted strongly with the rock cores during the tests, restricting their lateral expansion, and making resulting strength and Young's modulus measurements upper estimates of their in situ value. Apart from this discrepancy, measurement methods were in accord with those of the ISRM. The rock specimens were placed between steel end platens on a spherical seat in a testing machine, and LVDT strain gages measured both axial and diametric displacement. The Young's modulus was

Table 1
Results of the uniaxial compression tests. The sandstone has lower moduli and strength than the concretions, except for Concretion #1, which is weaker. These results are consistent with thin section and Schmidt hammer results, suggesting Concretion #1 is both petrologically and mechanically different than the other three concretion cores. The results for a partially calcite cemented rim surrounding some concretions is also included in the final row. Its static moduli are lower than Type 2 concretions, but its strength is comparable, and higher than the sandstone

Core sample	Description	Height/diameter	Compressive strength (MPa)	Young's modulus E (GPa)	Poisson ratio
S1	Sandstone	1.4	95	15	0.06
S2	Sandstone	1.4	121	21	0.14
S3	Concretion rim	2.3	142	33	0.07
S4	Sandstone	1.4	118	18	0.07
C1	Type 1 concretion	1.4	105	21	0.18
C2	Type 2 concretion	2.3	191	63	0.31
C3	Type 2 concretion	2.2	197	58	0.26
C4	Type 2 concretion	1.4	141	50	0.23

calculated from the slope of the linear portion of the resulting stress-strain curve, and the Poisson's ratio was calculated from:

$$\nu = -(\text{Young's modulus})/(\text{Slope of diametric}$$
$$\times \text{stress} - \text{strain curve}); \qquad (5)$$

where the slope of the diametric curve was negative.

As shown in Table 1, sandstone static moduli and strengths are less than the concretions, except for Sample C1, which has comparable strength. Considering the additional cementation found in the pore spaces of the concretion samples (Bessinger, 2000), it is likely that the additional calcite cement in the concretions stiffened grain contacts while more effectively redistributing axial loading stresses horizontally.

5.3. Brazilian tensile tests

Tensile strengths were determined indirectly via the Brazilian test. In these experiments a compressive stress applied as a line load induces tensile stresses in an orthogonal direction. In preparation for the experiments, samples were first machined to an approximate thickness to diameter ratio of 0.5:1, as recommended by ISRM (Bieniawski, 1978) (Table 2). Small pieces of paper were then placed in between the rock samples and steel platens to

distribute the load over a small arc and decrease the likelihood of shear failure initiating at the contacts (Jaeger and Cook, 1979). Finally, the tensile strength was calculated from the maximum load using the following equation:

Tensile strength
$$= (\text{Maximum load})/(\text{Thickness} \times \text{Diameter}). \qquad (6)$$

Table 2 shows that the concretions generally have a higher tensile strength than the sandstones, and that tensile strengths are an order of magnitude smaller than the compressive strengths.

5.4. Correlation of laboratory to field results

The coefficients of correlation between Schmidt rebound values obtained from the sandstone and concretions represented by Table 1 and the rock properties measured in the laboratory are summarized in Table 3. Coefficients are greater than 0.50, indicating a positive correlation. This is additional evidence that concretions with higher moduli are more likely to be fractured.

6. Analysis of concretion fracturing

6.1. Modeling method

Tensile and compressive far-field uniaxial stresses were applied to an isolated concretion in a numerical model to determine the conditions that could lead to the fractures observed in Fig. 2. Because these fractures are in the same orientation as the NW–SE joint set #1, jointing was subsequently inferred. The finite element code chosen for analysis was Ansys 5.4, which is capable of modeling elastic deformation and which can also solve for the stress and strains in three-dimensions by taking advantage of the symmetry imposed by spherical concretions. Modeled boundary conditions included an isolated concretion enclosed in a sandstone matrix extending six radii from

Table 2
Tensile strengths for the cores represented by the compression tests of Table 1. Concretion #1 is weaker than the sandstones, but the other concretions are stronger

Core sample	Description	Height/diameter	Brazilian strength (MPa)
S2	Sandstone	0.49	−11
S3	Concretion rim	0.48	−11
S4	Sandstone	0.49	−10
C1	Type 1 concretion	0.47	−9
C2	Type 2 concretion	0.48	−18
C3	Type 2 concretion	0.47	−15
C4	Type 2 concretion	0.49	−23

Table 3
Coefficients of correlation between the different rock properties measured in the field and in the laboratory. The amount of calcite cement (Bessinger, 2000) has a strong positive correlation with all of the other rock properties, suggesting it stiffens grain contacts. The Schmidt rebound number also has a positive correlation with the laboratory results. The Schmidt hammer correlations are used to estimate the moduli of the concretions in Fig. 14

	Calcite	Static Young's modulus	Unloading Young's modulus	Poisson ratio (v)	Compressive strength (Co)	Tensile strength (To)	Schmidt rebound number
Calcite	1.00						
Static Young's modulus	0.93	1.00					
Unloading Young's modulus	0.92	0.97	1.00				
Poisson ratio (v)	0.80	0.84	0.86	1.00			
Compressive strength (Co)	0.78	0.93	0.88	0.72	1.00		
Tensile strength (To)	0.83	0.77	0.77	0.64	0.50	1.00	
Schmidt rebound number	0.78	0.81	0.76	0.58	0.77	0.67	1.00

the concretion center. The error associated with not enclosing the concretion in an infinite medium was always less than 1.5%, as calculated by the analytical solution for an unfractured inclusion (Eshelby, 1957).

The first modeling assumption is that pore pressures and/or tectonic tensile stresses at the field site were operative. In the uniaxial tensile stress scenario considered below, these stresses were assumed to be sufficient to directly cause concretion fracturing. In the uniaxial compressive stress scenario, these stresses were assumed to reduce the confining stress acting against crack dilation, allowing a uniaxial compressive stress to be applied along the boundary of the modeled region.

Because the length-to-diameter ratios of the cores measured in laboratory compression experiments are different, moduli and strengths of the samples cannot be directly compared. Nevertheless, average values from Type 2 concretions were used for analysis (Table 4), with the explicit understanding that the results are not necessarily representative of the magnitude of the stresses during jointing. A sensitivity test was included to incorporate the possibility that the moduli and strengths during fracturing were different than the average laboratory value.

6.2. CASE #1: tensile loading

The uniaxial tensile loading stress applied to the concretion and matrix in this case was -10.6 MPa, or the mean tensile strength of the sandstone. The objective of using this value was to analyze the static case where the stress is sufficient to cause sandstone jointing.

The tensile stress within and adjacent to a Type 2 concretion under an applied uniaxial tensile stress is shown in Fig. 11a. Using dashed horizontal lines to delineate the stresses leading to sandstone and concretion fracture, fracturing is predicted for the three-dimensional case in the concretion and in the sandstone directly adjacent to it. By contrast, the two-dimensional plane strain case does not produce enough stress to preferentially fracture the concretion.

Because the stress in the sandstone outside of the concretion along the x-axis is the same as the stress within the concretion, debonding of the concretion from the sandstone is predicted to precede concretion fracturing. Fig. 14b shows the state of stress along both the x- and y-axes for the case where debonding fractures on either side of the concretion has extended a distance of one diameter from the edge. As shown in the figure, the tensile stress is smaller than the tensile strength of the concretion.

Based on these results, the only explanation for concretion fracturing under uniaxial tensile stresses applied perpendicular to the crack face is that fracture growth occurred subcritically. Under these conditions, the sensitivity of crack growth to the stress concentration factor is measured by the stress corrosion exponent (n), which is diminished by adsorption and/or dissolution reactions

Table 4
Summary of the rock properties used in the numerical simulations. The values for Concretion Type 1, Concretion Type 2, and the Sandstone are based on the mean values determined in the laboratory. The properties for the Sandstone in the sensitivity test were taken from (Touloukian et al., 1989) to represent the condition where the sandstone is not completely lithified

Material property	Concretion Type 2	Laboratory test sandstone	Sensitivity test sandstone
E (MPa)	57	18	10
v	0.27	0.09	0.32
σ_C (MPa)	177 ± 25	112 ± 12	91
σ_T (MPa)	-18 ± 3	-11 ± 0.4	-10

occurring at the crack tip. The problem with this explanation is that Renshaw and Pollard (1994) demonstrated that multiple joints can only form either by employing constant strain boundary conditions and/or stress corrosion indices that are several orders of magnitude lower than have been produced experimentally. Crack growth at a value for (n) this small occurs essentially in the absence of any stress

concentration at the tip, and has not been demonstrated for rock (Atkinson and Meredith, 1987).

6.3. CASE #2: compressive loading

Due to the difficulty in eliminating end effects in laboratory uniaxial compressive strength tests, there have
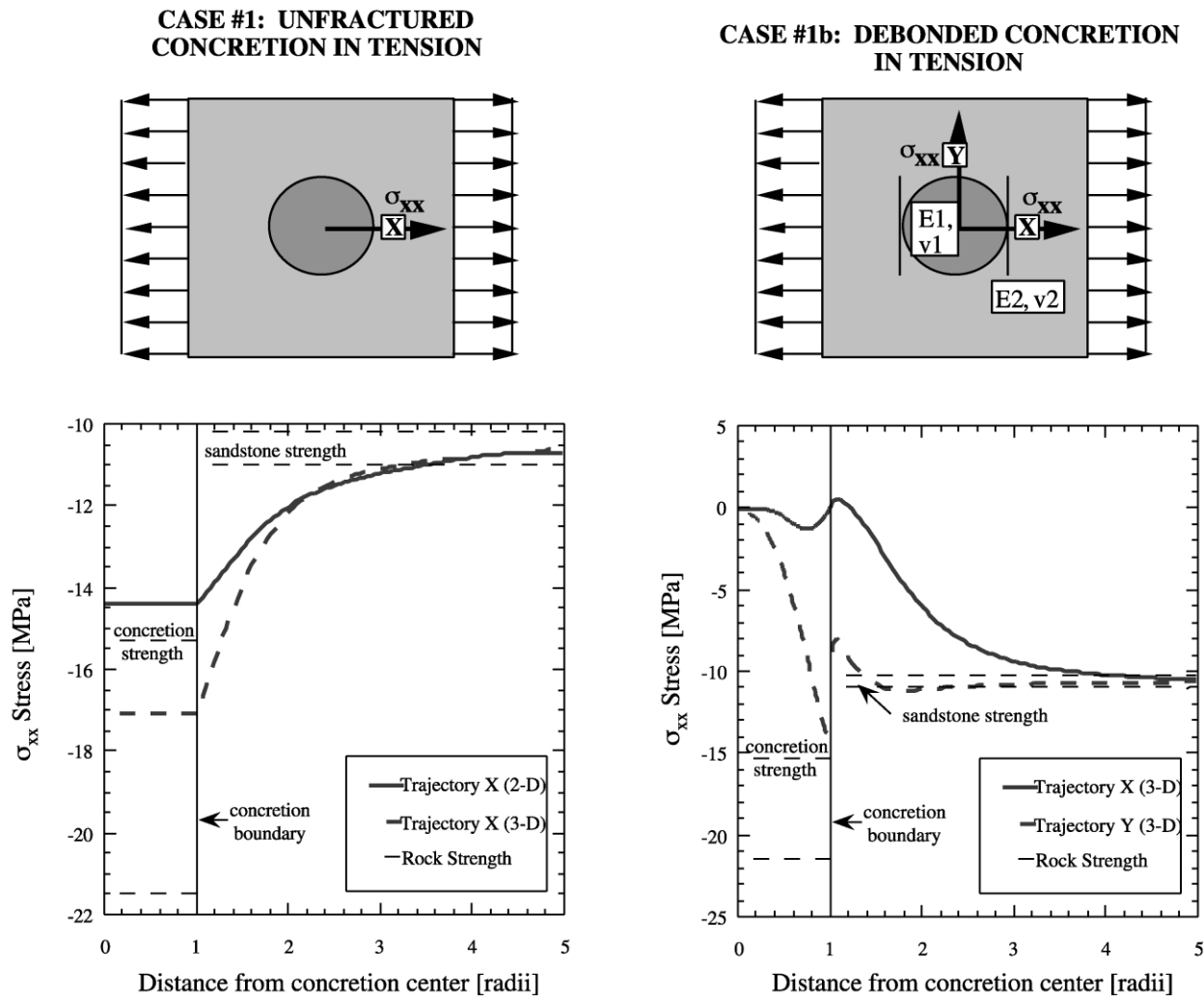

Fig. 11. Results of the numerical experiments for the case where tensile loading stresses are applied. The top figure depicts the loading cases and the location of any fractures within and around the concretions. The lower plots show the σ_{xx} stress versus distance along the x-axis from the concretion center. The upper and lower limits for the strength of the sandstone and concretion are from one standard deviation in the measured laboratory values. (a) For the unfractured concretion, a stress concentration occurs within the concretion and along the contact with the sandstone. (b) The stress at the debonding fracture is zero along the x-axis and the stress inside of the concretion is significantly below its strength.

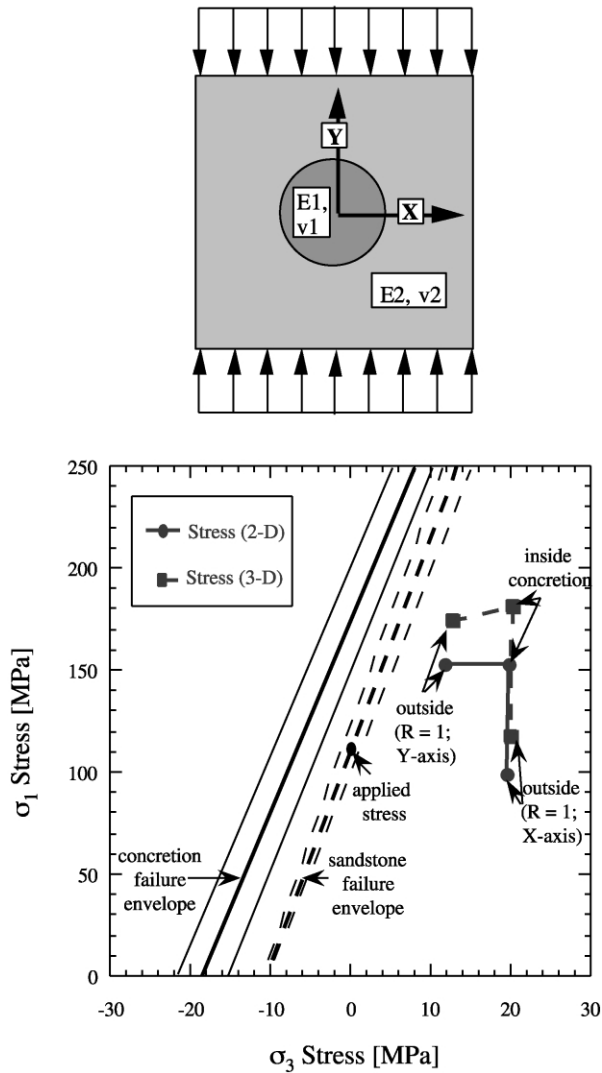## CASE #2: UNFRACTURED CONCRETION IN COMPRESSION

Fig. 12. Stress field inside of a concretion under uniaxial compressive loading. The depicted scenarios are shown in the top figures. The lower plots show the σ_1 and σ_3 state of stress inside each concretion and at the contact with the sandstone. The stress at any particular point is displayed relative to a linear fracture envelope defined by the tensile and compressive strengths measured in the laboratory. The standard deviations for the concretions are drawn as solid lines and the standard deviations for the sandstone are drawn with dashed lines. In the lower part, the two-dimensional plane strain and three-dimensional cases for an unfractured concretion are shown. Because the stress field is uniform, only the stress in the center and at the boundary at the x- and y-axes are shown. The stresses lie below the failure envelope and no fracturing is predicted.

been relatively few studies that provide information regarding compression-driven tensile fracturing under geologic conditions. Because Jaeger and Cook (1963) demonstrated through a series of biaxial compressive stress experiments that fractures can form independently of end effects near the uniaxial compressive strength of the rock, failure criteria was defined in this study using linear failure envelopes drawn between the laboratory compressive and tensile strengths measured in the laboratory. Without having

measured a compression-driven tensile failure envelope using the biaxial load cell of Jaeger and Cook (1963), the shape of a failure envelope is debatable; however, there is some theoretical and experimental evidence to suggest that it is linear (Jaeger and Cook, 1979).

The stress inside a concretion, and along the concretion/sandstone interface, is shown for the case of a simulated two- and three-dimensional concretion loaded by a 112 MPa uniaxial compressive load applied along the y-axis in Fig. 12a. Also illustrated in the figure are two linear failure envelopes for the concretion and sandstone, each representing one standard deviation in the strength measurements. According to the figure, confining stresses in the minimum principal stress direction prevent fracturing inside the concretion. This stress is due to the larger Poisson's ratio of the concretion.

6.4. CASE #3: sensitivity analysis

A third possible fracturing scenario is that fracturing occurred during burial when the sandstone had different material properties than those measured in the laboratory. Price (1974) used low values of the Young's modulus and high values for the Poisson's ratio to account for the effects of thermal strains and incomplete lithification of the sediments. These processes were modeled by assigning the sandstone the properties reported in Table 4 (Touloukian et al., 1989). This sandstone has a lower Young's modulus and strength than measured in this study, but a higher Poisson's ratio (the concretion values were retained in the analysis based on their origin early in diagenesis).

Fig. 13a shows the state of stress in and adjacent to a concretion for a uniaxial and biaxial applied compressive stress of 91.2 MPa. Also shown are results for both two-dimensional plane strain and three-dimensional boundary conditions. According to the results, all three cases in this figure lead to preferential concretion fracturing because the larger Poisson's ratio of the sandstone generates tensile stresses internal to the concretion.

Because only three-dimensional boundary conditions result in preferential debonding of the concretion from the matrix, these conditions were simulated in two dimensions for the case where debonding occurred by shifting the concretion failure envelope to the right a distance equivalent to the distance between the two- and three-dimensional concretion simulations in Fig. 13a. Fig. 13b shows the subsequent stresses inside a concretion after a debonding fracture has grown a length of one concretion diameter on either side. Assuming that one fracture is able to extend across the concretion, additional fracturing is still possible (Fig. 13c). The region most favorable to additional fracturing is the concretion center along the X1 trajectory. As more fractures form within the concretions, the potential for additional failure is reduced (Fig. 13d).
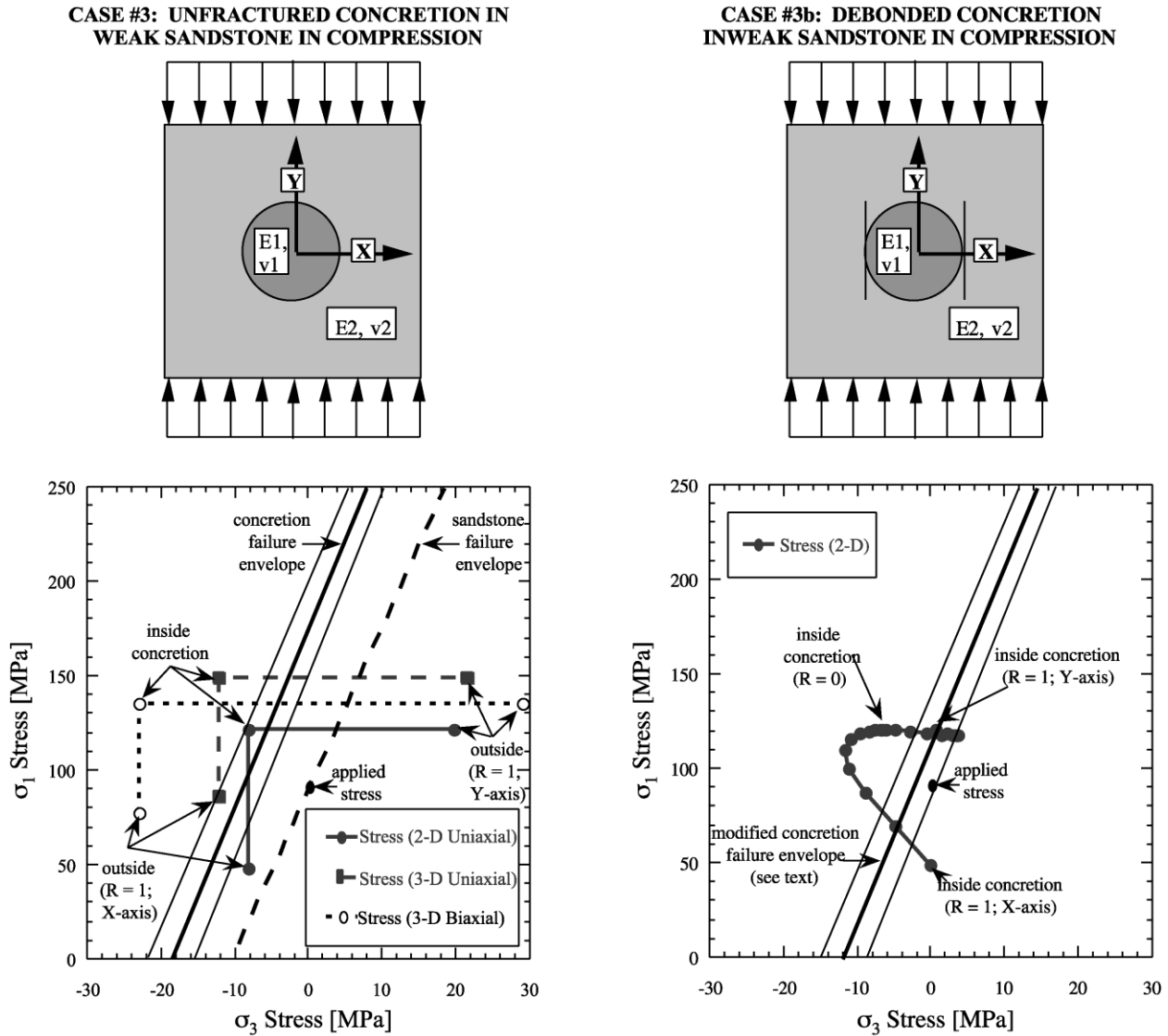
Fig. 13. Stress field inside of concretions if the sandstone has a higher Poisson ratio and lower Young's modulus and strength than the sandstone. (a) Stress inside an unfractured concretion for three different boundary conditions. The stresses greatly exceed the concretion failure envelope. (b) Case of a debonded concretion. Point A represents the stress along the y-axis at the boundary of the concretion when debonding has initiated but has not yet extended into the sandstone matrix as it has in the illustration above the plot. (c) Stress after an internal fracture is added to the model. Along the × 2 trajectory the σ_3 confining stress initially increases and then re-approaches zero as indicated by the arrows. (d) Three internal fractures and two debonding fractures. The additional fractures break up the stress field and make additional fracturing more likely along trajectory × 2.

6.5. Summary of concretion fracturing mechanisms

It is very difficult to explain the origin of the concretion fractures using the rock properties measured in the laboratory. A uniaxial tensile stress favors concretion debonding from the sandstone matrix without generating internal fractures. A uniaxial compressive stress inhibits fracturing in the high modulus concretions because the Poisson's ratios are larger than the sandstone. An alternative scenario is that fracturing occurred during burial of the sedimentary rock, while the sandstone was still incompletely lithified. Using the rock property values in Table 4, a uniaxial compressive stress can cause multiple internal

fractures due to generated tensile stresses. As more fractures form, tensile stresses are replaced by nearly uniaxial compressive stress conditions. This suggests that a finite number of concretion fractures are possible until additional fractures are formed by another mechanism, such as grain-scale compression-driven fracturing.

7. Analysis of sandstone jointing

7.1. Modeling method

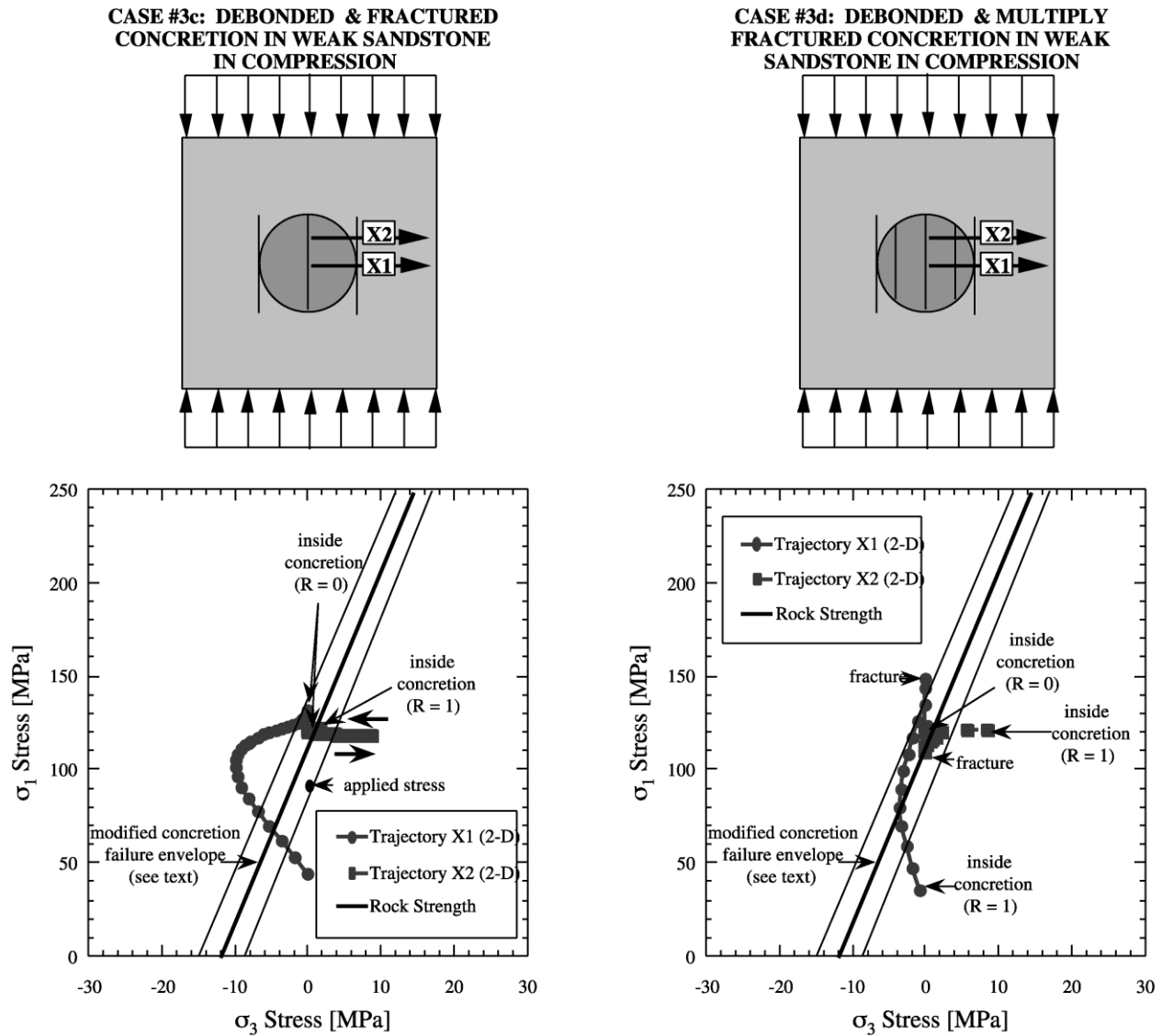Considering that applied uniaxial compressive stresses

Fig. 13 (*continued*)

are more compatible with the observation of concretion fractures, numerical simulations were performed to determine how they may have interacted with the concretions in the field to generate joint set #1 in Area 9 (Fig. 14). This particular area of the field site has several Type 2 concretions and three primary joints, all initiating in the vicinity of the boundary between sandstone and concretions. The first joint is adjacent to concretion #4 and extends several diameters on either side of it. The other two joints are associated with concretion #3. One joint extends through the boundary of Area 9. The other joint is subparallel to the first, and initiates on the other side of concretion #3. Only a portion of this joint is shown (at approximately 250 m in the figure).

In the first simulation in this study, uniaxial compressive stresses were applied along the top and bottom boundaries of a meshed grid containing no fractures. In a second model run, a single joint was included that bisects the area. The properties of the concretions used in this analysis were taken from measured Schmidt rebound values and a linear correlation with laboratory elastic moduli. Sandstone properties were assumed to be equivalent to the sensitivity test sandstone in Table 4. Most of the concretions have Young's moduli and Poisson's ratios higher than the sandstone. The exceptions are concretions #10 and #12. The modeled region shown in Fig. 14 was enclosed in a surrounding sandstone medium to isolate it from boundary effects, and was pinned on one corner and isolated from rigid body motion by a roller on another.

7.2. Model results

Fig. 15a shows the predicted σ_{xx} stress in Area 9 under a uniaxial compressive loading stress of 112 MPa applied in
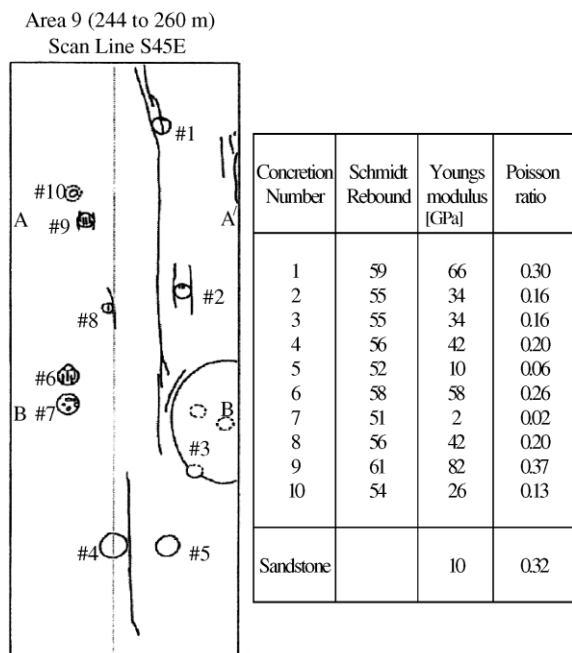
Fig. 14. Map of Area 9 where numerical modeling of jointing was performed. The table next to the figure reports the Schmidt rebound values and elastic moduli used for each of the concretions numbered in the plot. The values for the sandstone are those of the sensitivity test from Table 4.

Concretion Number	Schmidt Rebound	Youngs modulus [GPa]	Poisson ratio
1	59	66	0.30
2	55	34	0.16
3	55	34	0.16
4	56	42	0.20
5	52	10	0.06
6	58	58	0.26
7	51	2	0.02
8	56	42	0.20
9	61	82	0.37
10	54	26	0.13
Sandstone		10	0.32

the direction of the y-axis. Along the trajectory A–A′ in Fig. 15a, tensile stresses are greatest outside of concretion #9, but smaller inside because the Poisson's ratio is higher than the sandstone. Stresses are relatively unaffected by the presence of fracturing in the sandstone.

Along trajectory B–B′ in Fig. 15b, tensile stresses are generated outside of concretion #7 because of the Poisson's ratio mismatch. After inclusion of the modeled joint, tensile stresses are still large enough to generate the joint observed on the right side of concretion #3.

Combining these results, compression-driven tensile stresses are predicted to be large enough to cause jointing on both sides of concretion #3. By contrast, extension of these joints in the vicinity of A–A′ occurs under very low tensile stresses acting perpendicular to the joints. Consequently, after initial compression-driven tensile fracturing has occurred near the stiff concretion, additional jointing occurs under nearly uniaxial compressive stress conditions. Laboratory evidence of Jaeger and Cook (1963) suggests that the mechanism leading to extension in this region is grain-scale compression-driven tensile fracturing.

7.3. Origin of jointing stresses

During burial, far field tensile stresses necessary to produce stress anisotropy develop due to the fact that the surface of the Earth is curved and that for a sedimentary basin of length AC (Fig. 16), extension occurs during burial below length ABC (Price, 1974). Using equations relating basin length (L), the radius of the Earth (R), depth to
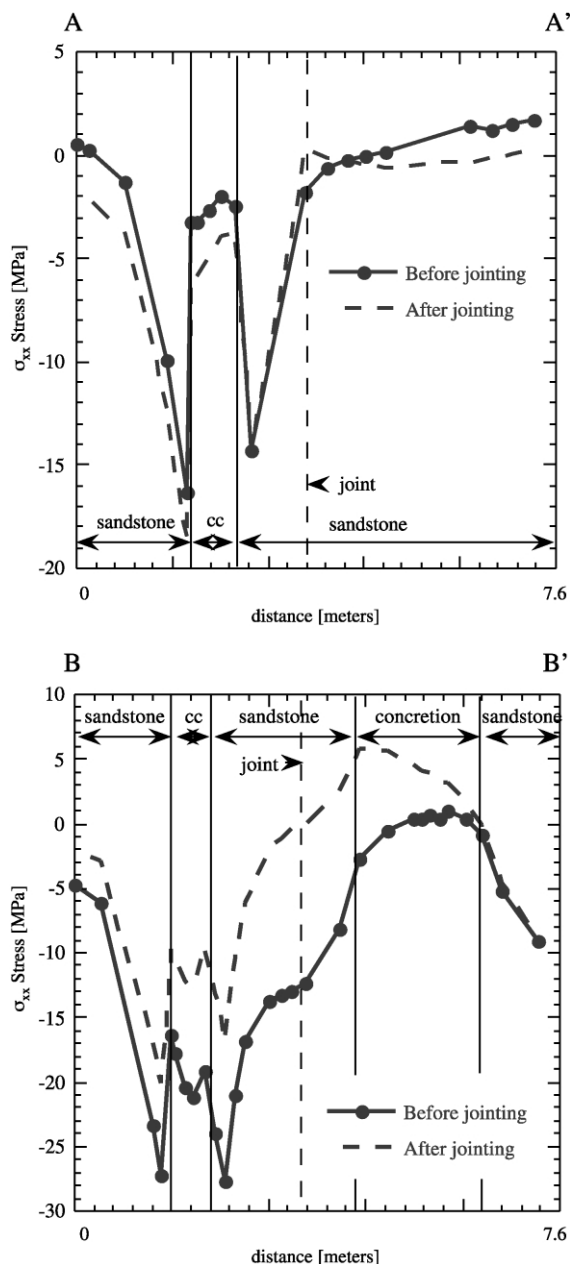

Fig. 15. The σ_{xx} stress field for the case of the weak sandstone after far field uniaxial compressive stresses have been applied in the vertical direction along a bordered region surrounding the area. (a) Tensile stresses are generated in both the concretions and sandstone, but are localized in the vicinity of the concretions. (b) After one joint is allowed to extend all the way through the middle of the region, the tensile stresses are only slightly reduced in the vicinity of the concretions.

maximum compression (z), and total strain (e), and estimated basin dimensions of 230 km by 120–130 km (Mustard, 1994), after just 0.28 km of burial, the short axis of the basin at Vancouver Island is predicted to have undergone extension. Assuming the DeCourcy Formation was buried approximately 3 km (England, 1990), the total tensile strain would be -1.2×10^{-3} and -2.1×10^{-4} for the short and long axes, respectively.
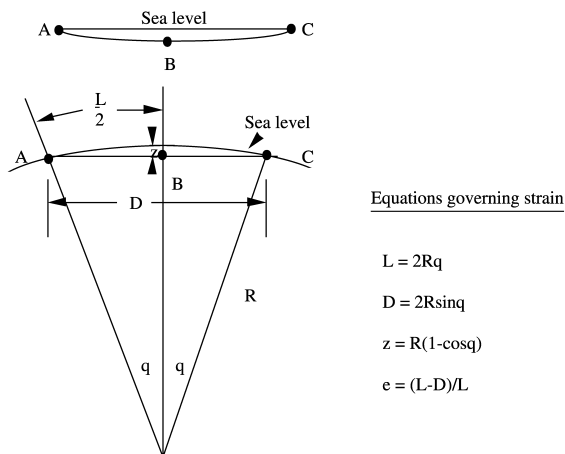
Fig. 16. Illustration of how tensile strains can be generated in a downwarping basin (after Price, 1974). The basin appears concave, but relative to the dimensions of the Earth it is convex. Consequently, as it is buried to line ABC it is compressed, but thereafter it is in extension. The depth to this confinement zone (z) is only 0.28 km for the short axis of the Nanaimo Basin on Vancouver Island. The equations relating strain to the dimensions of the basin and Earth are shown to the right of the figure.

The combined equations utilized by Price (1974) to explain the effective horizontal stresses in a downwarping basin such as this are given by:

$$\sigma'_x = \frac{\upsilon}{(1-\upsilon)}\sigma_z - \epsilon_x E - p; \tag{7}$$

$$\sigma'_y = \frac{\upsilon}{(1-\upsilon)}\sigma_z - \epsilon_y E - p; \tag{8}$$

where cross strain terms were neglected without introducing significant error. Based on the effective stress law as re-
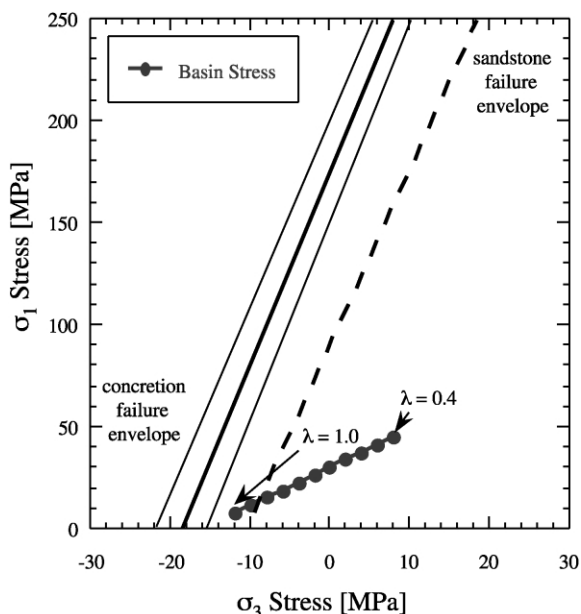

Fig. 17. Calculated effective stresses in the Nanaimo Basin assuming uniaxial strain conditions and a lambda parameter ranging from 0.4 to 1.0. The stress is only large enough to cause jointing at a high value for lambda. Because the compressive loading stress under such a condition is very small, a tectonic component is necessary for jointing.

stated in Eq. (1), an increase in pore pressure also contributes to the total stress (s) such that a correct expression of Eq. (7) is:

$$\sigma'_x = \frac{\upsilon}{(1-\upsilon)}(\sigma_z - p) - \epsilon_x E; \tag{9}$$

$$\sigma'_y = \frac{\upsilon}{(1-\upsilon)}(\sigma_z - p) - \epsilon_y E; \tag{10}$$

Fig. 17 shows the corresponding state of stress for the DeCourcy Formation at Vancouver Island, assuming an average density of 2.5 g/cm^3 for the overlying sediments and using the average rock properties during burial given in Table 4. The parameter (λ) measures the ratio of pore pressure to the vertical gravitational loading stress. For the short axis of the basin to have experienced effective tensile stresses a value of (λ) of 0.65 would have had to occur (the long axis of the basin would have experienced tensile effective stresses as the ratio of pore pressure to vertical pressure approached 0.95). Because the resultant basin stresses are not large enough to preferentially fracture the concretions (Fig. 17), it is difficult to explain jointing in the absence of a tectonic stress component.

8. Unresolved issues

One uncertainty in this study is the rock properties at the time of fracturing. This includes the Poisson's ratio, which greatly affects the state of stress within the concretions. The stresses are also probably less than those required to break the rock in the laboratory due to subcritical crack growth, higher temperatures, and lower strain rates (Paterson, 1978).

A second set of unresolved issues are those associated with the properties of compression-driven tensile fracturing. Additional laboratory testing under biaxial stresses imposed by the load cell of Jaeger and Cook (1963) are required to yield a 'true' compression-driven tensile fracturing failure envelope. Also, the factors controlling the spacing of laboratory and field compression-driven tensile fractures are unknown. In cases where boundaries are fixed such as biaxial test cells, dilation must be accommodated entirely by elastic deformation. Given that the compliance of a rock core of axial dimension (l) is:

$$1/\kappa = (\epsilon_3 \times l)/\sigma_3, \tag{11}$$

where (κ) is the stiffness, (ϵ_3) is the axial strain, and (σ_3) is the minimum confining stress, under zero axial displacement, the compliance of the system in the direction of fracture dilation is zero because (ϵ_3) is zero. Consequently, the number of fractures that can grow is limited.

9. Conclusions

The relative importance of joint-parallel compressive stresses in jointing was investigated at a field site on

Vancouver Island, British Columbia. This field site is unique in that it contains paleostress indicators in the form of fractured calcareous concretions that were used to deduce the combination of stresses responsible for joint set #1 in the surrounding sandstone. Assuming the Poisson's ratio of the sandstone was higher than the concretion during fracturing, compression-driven tensile stresses would have been capable of producing the observed fractures in the calcareous concretions. They also would have seeded the field site with a small population of joints. Extension of joints into areas with fewer concretions would occur under nearly uniaxial compressive stresses, presumably due to grain-scale compression-driven tensile stresses. Further studies must address the mechanics of initiation, propagation, termination, and spacing of joints formed under geologic compressive stresses.

Acknowledgements

References

Atkinson, B.K., Meredith, P.G., 1987. The theory of subcritical crack growth with applications to minerals and rocks. In: Atkinson, B.K., (Ed.), Fracture Mechanics of Rock, Academic Press, London, pp. 111–166.

Atkinson, R.H., 1978. Suggested methods for determining hardness and abrasiveness of rocks. International Journal of Rock Mechanics and Mining Science 15, 89–97.

Bai, T., Pollard, D.D., 2000. Fracture spacing in layered rock: a new explanation based on the stress transition. Journal of Structural Geology 22, 43–57.

Bessinger, B.A., 2000. The geochemistry of gold, arsenic, and antimony in the Carlin-type gold deposits and the mechanics of geologic fractures. Ph.D. thesis, University of California at Berkeley.

Bieniawski, Z.T., 1978. Suggested methods for determining tensile strength of rock materials. International Journal of Rock Mechanics and Mining Science 15, 99–103.

Bieniawski, Z.T., 1979. Suggested methods for determining the uniaxial compressive strength and deformability of rock materials. International Journal of Rock Mechanics and Mining Science 16, 135–140.

Cruikshank, K.M., Zhao, G., Johnson, A.M., 1991. Analysis of minor fractures associated with joints and faulted joints. Journal of Structural Geology 13, 865–886.

Eidelman, A., Reches, Z., 1992. Fractured pebbles—a new stress indicator. Geology 20, 307–310.

Engelder, T., Lacazette, A., 1990. Natural Hydraulic Fracturing. International Symposium on Rock Joints. Leon, Norway.

England, T.D.J., 1990. Late Cretaceous to Paleogene evolution of the Georgia Basin, southwestern British Columbia. Ph.D. thesis, Memorial University of Newfoundland.

England, T.D.J., Calon, T.J., 1991. The Cowichan fold and thrust system, Vancouver Island, southwestern British Columbia. Bulletin of the Geological Society, America 103, 336–362.

Eshelby, J.D., 1957. The determination of the elastic field of an ellipsoidal inclusion and related problems. Proceedings of the Royal Society, London Series A 241, 376–396.

Goodman, R.E., 1993. Engineering Geology: Rock in Engineering Construction, John Wiley, New York.

Huang, Q., Angelier, J., 1989. Fracture spacing and its relation to bed thickness. Geology Magazine 126, 355–362.

Hucka, V., 1965. A rapid method for determining the strength of rocks in situ. International Journal of Rock Mechanics and Mining Science 2, 127–134.

Jaeger, J.C., Cook, N.G.W., 1963. Pinching-off and disking of rock. Journal of Geophysical Research 68, 1759–1765.

Jaeger, J.C., Cook, N.G.W., 1979. Fundamentals of Rock Mechanics, Chapman and Hall, London.

Kemeny, J., Cook, N.G.W., 1985. Formation and stability of steeply dipping joint sets. 26th Symposium on Rock Mechanics, pp. 471–478.

Kemeny, J., Cook, N.G.W., 1987. Determination of rock fracture parameters from crack models for failure under compression. 28th Symposium on Rock Mechanics, pp. 367–374.

Lorenz, J.C., Teufel, L.W., Warpinski, N.R., 1991. Regional fractures I: a mechanism for the formation of regional fractures at depth in flat-lying reservoirs. American Association of Petroleum Geology Bulletin 75, 1714–1737.

McCarroll, D., 1987. The Schmidt hammer in geomorphology; five sources of instrument error. Technical Bulletin—British Geomorphology Research 36, 16–27.

Mustard, P.S., 1994. The Upper Cretaceous Nanaimo Group, Georgia Basin. Bulletin of Geological Surveyors, Canada 481, 27–95.

Nur, A., 1982. The origin of tensile fracture lineaments. Journal of Structural Geology 4, 31–40.

Olson, J.E., 1993. Joint pattern development: effect of subcritical crack growth and mechanical interaction. Journal of Geophysical Research 98, 12251–12265.

Paterson, M.S., 1978. Experimental Rock Deformation—the Brittle Field, Springer-Verlag, New York.

Pollard, D.D., Aydin, A., 1988. Progress in understanding jointing over the past century. Bulletin of the Geological Society, America 100, 1181–1204.

Pollard, D.D., Segall, P., 1987. Theoretical displacements and stresses near fractures in rock. In: Atkinson, B.K., (Ed.), Fracture Mechanics of Rock, Academic Press, London, pp. 247–349.

Poole, R.W., Farmer, I.W., 1980. Consistency and repeatability of Schmidt hammer rebound data during field testing. International Journal of Rock Mechanics and Mining Science 17, 167–171.

Price, N.J., 1974. The development of stress systems and fracture patterns in undeformed sediments. Proceedings of the Third International Conference of the Society of Rock Mechanics, pp. 487–519.

Price, N.J., Cosgrove, J.W., 1990. Analysis of Geological Structures, Cambridge University Press, Cambridge.

Renshaw, C.E., Pollard, D.D., 1994. Numerical simulation of fracture set formation: a fracture mechanics model consistent with experimental observations. Journal of Geophysical Research 99, 9359–9372.

Renshaw, C.E., Pollard, D.D., 1995. An experimentally verified criterion for propagation across unbounded frictional interfaces in brittle, linear

elastic materials. International Journal of Rock Mechanics and Mining Science 32, 237–249.

Secor, D., 1965. Fluid pressure in jointing. American Journal of Science 263, 633–728.

Segall, P., Pollard, D.D., 1983. Joint formation in granitic rocks of the Sierra Nevada. Bulletin of the Geological Society, America 94, 563–575.

Suppe, J., 1985. Principles of Structural Geology, Prentice-Hall, Englewood Cliffs, NJ.

Touloukian, Y.S., Judd, W.R., Roy, R.F., 1989. Physical properties of rocks and minerals. CINDAS Data Series on Material Properties V, p. II-2.

Wu, H., Pollard, D.D., 1995. An experimental study of the relationship between joint spacing and layer thickness. Journal of Structural Geology 17, 887–905.